

FIG. 2: (a) Nonlinear kinetic function  $f(a, u)$  for different values of voltage  $u$ , (b) diffusion coefficient  $D(a)$  as a function of the electron density  $a$  (double-logarithmic scale), (c) current-voltage characteristic for spatially homogeneous states (solid line) and filamentary states (dashed line) for  $L = 30$ ; load line for  $U_0 = -84.2895$ ,  $r = -35$  (dotted line), (d) spatial profile of a half filament,  $a(x)$  (solid line) and  $j(x)$  (dotted line) ( $L = 30$ ;  $u = 265$ )

in the  $x - y$  plane. The spatially homogeneous steady states give rise to a Z-shaped current-voltage characteristic [26] exhibiting bistability in a range of applied voltages. The middle branch of the current-voltage characteristic can be stabilized by applying an appropriate active circuit with a negative load resistance [27]. Complex spatio-temporal patterns can arise if the lateral redistribution of electrons within the quantum well [20–25, 28] is taken into account. In the following we assume that the extension of the device in  $y$ -direction is small and charge inhomogeneities can only appear in the  $x$ -direction. Using dimensionless variables throughout we arrive at the following equations:

$$\frac{\partial a}{\partial t} = \frac{\partial}{\partial x} \left( D(a) \frac{\partial a}{\partial x} \right) + f(a, u) - K F_a(x, t) \quad (1)$$

$$\frac{du}{dt} = \frac{1}{\varepsilon} (U_0 - u - r \langle j \rangle) - K F_u(t) \quad (2)$$

Here the uncontrolled model [25] has been extended by the control terms  $K F_a$  and  $K F_u$  representing the con-

trol forces with amplitude  $K$ . The dynamic variables are the inhibitor  $u(t)$  and the activator  $a(x, t)$ . The one-dimensional spatial coordinate  $x$  corresponds to the direction transverse to the current flow. In the semiconductor context  $u(t)$  denotes the voltage drop across the device and  $a(x, t)$  is the electron density in the quantum well. The nonlinear, nonmonotonic function  $f(a, u)$  describes the balance of the incoming and outgoing current densities in the quantum well (Fig. 2 (a)), and  $D(a)$  is an effective, electron density dependent transverse diffusion coefficient (Fig. 2 (b)) [29]. The local current density in the device is  $j(a, u) = \frac{1}{2}(f(a, u) + 2a)$ , and  $\langle j \rangle = \frac{1}{L} \int_0^L j dx$  is associated with the global current. Eq. (2) represents Kirchoff's law of the circuit in which the device is operated. The external bias voltage  $U_0$ , the load resistance  $r$ , and the time-scale ratio  $\varepsilon$  are dimensionless external parameters. We consider a system of width  $L$  with no charge transfer through the lateral boundaries (i.e., Neumann boundary conditions  $\partial_x a = 0$  at  $x = 0, L$ ). In Appendix A we give explicit expressions for  $f(a, u)$  and  $D(a)$  and draw the connection to the microscopic physical parameters.

In the case without control force ( $K = 0$ ) one stationary solution of (1) is given by the homogeneous solution  $a(x) = a_i^{\text{hom}}$  with  $f(a_i^{\text{hom}}, u) = 0$ . Up to three different solutions  $a_i^{\text{hom}}$  may exist for one fixed value of  $u$  (Fig. 2(a)). This gives rise to a Z-shaped current-voltage characteristic  $j(u) = a$  (solid line in Fig. 2(c)).

The spatially homogeneous stationary solutions of the coupled equations (1) and (2) are given by the intersection of the current-voltage characteristic  $j(u)$  and the load line which is the nullcline  $\langle j \rangle = (U_0 - u)/r$  of (2). States on the middle branch of the  $j(u)$  characteristic are unstable in a passive external circuit with effective resistance  $r > 0$ . By choosing  $r < 0$ , which can be realised by an active circuit, i.e. applying an additional control voltage proportional to the device current  $\langle j \rangle$  in series with the bias  $U_0$  [27], it is in principle possible to stabilize the middle branch of the stationary  $j(u)$  characteristic and access it experimentally, but for large enough  $\varepsilon$  Hopf bifurcations can occur, leading to uniform limit cycle oscillations of the current and voltage.

It should be noted that, depending upon the intersection of the load line with the  $j(u)$  characteristics, the DBRT represents either a bistable, or an oscillatory, or an excitable active medium [30]. It is remarkable that the DBRT can be operated as an excitable system even in the spatially homogeneous case. Consider the situation in Fig. 3(a) where the load line intersects the homogeneous characteristic near the second turning point at a low current value ( $j \approx 4.63$ , and  $\varepsilon = 70$ ). Due to the large value of  $\varepsilon$  the relaxation in  $u$  is much slower than the relaxation in  $a$ . If noise pushes the system off its fixed point in the low current regime, it quickly relaxes to a value of  $a \equiv j$  in a high current state. Then the slow relaxation in  $u$  sets in and drags the system along the homogeneous characteristic towards high  $u$  (since we are above the load line) until the upper branch of the

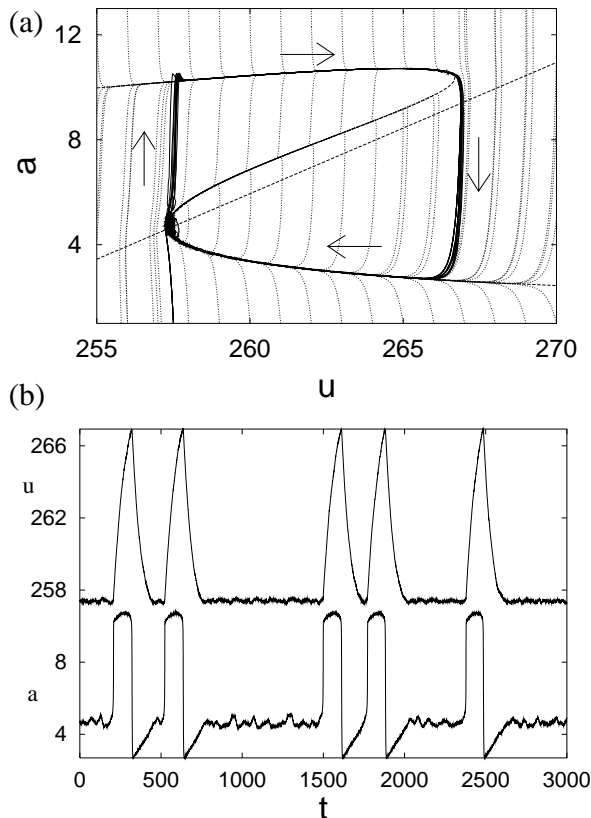


FIG. 3: DBRT in the excitable regime: (a) Spatially homogeneous phase portrait of electron density  $a$  vs. voltage  $u$  for  $r = -2$ ,  $U_0 = 248.11$ ,  $L = 30$ ,  $\varepsilon = 70$ . Solid line: trajectory of the system under noise. Dashed lines: Load line (straight) and homogeneous current–voltage characteristic ( $Z$ -shaped). Dotted lines: phase flow of the system. (b) Response of  $a$  and  $u$  triggered by noise.

homogeneous characteristic ends. At this point, the system again quickly relaxes in  $a$ , this time towards a low current state. Since we are now below the load line the system finally returns to the fixed point. This excursion in phase space results in a spike-like response in the current and voltage signal upon external noise (Fig. 3(b)) which is characteristic for an *excitable* medium.

### III. SPATIO-TEMPORAL SCENARIOS

As the device width  $L$  in  $x$ -direction increases (the device width in  $y$  direction is fixed and small compared to  $L$ ), the middle branch of the homogeneous solution  $a_2^{hom}$  (Fig. 2(c)) becomes unstable against inhomogeneous fluctuations. A straightforward linear stability analysis [19] shows that this occurs at

$$L > \pi \sqrt{\left| \frac{D(a_2^{hom})}{\partial_a f(a_2^{hom})} \right|}. \quad (3)$$

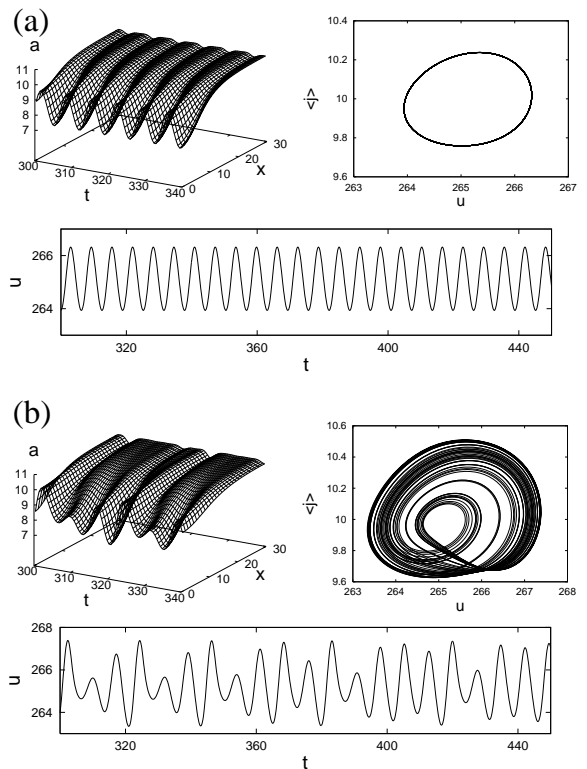


FIG. 4: Spatio-temporal breathing patterns: electron density evolution, phase portrait, and voltage time series for (a)  $\varepsilon = 7.0$ : periodic breathing, (b)  $\varepsilon = 9.1$ : chaotic breathing; load line as in Fig. 2

Then an additional stationary solution of eq. (1) arises in the form of a current filament. Fig. 2(d) shows the dependence of  $a$  and  $j$  on the transverse spatial coordinate  $x$  for a half-filament with  $L = 30$  and  $u = 265$ . The dashed line in Fig. 2(c) depicts the corresponding current–voltage characteristic  $\langle j \rangle(u)$ .

The filament is stable for  $r < 0$  at small  $\varepsilon$ , but becomes unstable by a Hopf bifurcation for large enough  $\varepsilon$ . In this case complex spatio-temporal breathing (Fig. 4) and spiking patterns (Fig. 5) are expected if the homogeneous fixed point is still stable with respect to Hopf bifurcations [31].

Choosing the load line as in Fig. 2(c) (dotted line), the homogeneous fixed point on the middle branch is always unstable against the filamentary mode for  $L = 30$ , but is stable against Hopf bifurcations up to  $\varepsilon < 16.43$  (dotted line in Fig. 6). On the other hand, a Hopf bifurcation of the half-filament occurs already at  $\varepsilon_h^f = 6.4$ , leading to periodic filament oscillations (Fig. 4(a)) for  $\varepsilon > \varepsilon_h^f$ . This *breathing* filament undergoes a period doubling cascade for  $\varepsilon > 8.2$  leading to chaos (c.f. Fig. 4(b)). We note that the dynamic behavior is characterized by oscillations of varying amplitude around the unstable filamentary fixed point, which is typical for a chaotic breathing scenario.

With further increase of  $\varepsilon$  oscillations around the ho-

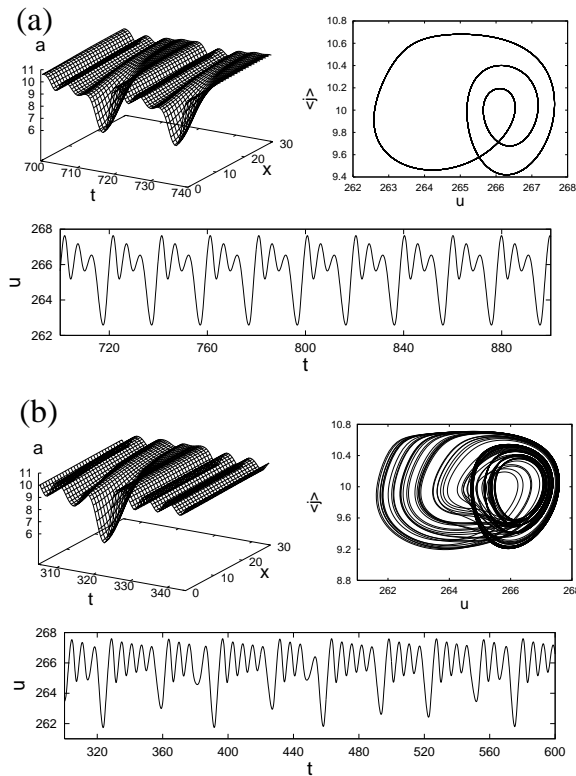


FIG. 5: Spatio-temporal spiking patterns: as in Fig. 4 but (a)  $\varepsilon = 13.15$ : periodic spiking, (b)  $\varepsilon = 16.5$ : chaotic spiking.

homogeneous fixed point become important and a competition between the two fixed points sets in. Thereby the breathing filament transmutes into a spiking filament as in Fig. 5(a) for  $\varepsilon = 13.15$ . Here two oscillations around the homogeneous fixed point are followed by one oscillation around the filamentary fixed point. This periodic spiking quickly becomes chaotic at further increase of  $\varepsilon$ , yielding a chaotic spiking behaviour, which is characterized by a sequence of almost homogeneous oscillations intermitted by one large filamentary oscillation (Fig. 5(b)). The resulting phase portrait is reminiscent of the Rössler attractor. While breathing oscillations are always close to the filamentary fixed point, the spiking oscillations are related to both the filamentary and the homogeneous fixed point. The complete bifurcation diagram with respect to  $\varepsilon$  is depicted in Fig. 6. We note that the homogeneous limit cycle emerging from a Hopf bifurcation of the homogeneous fixed point (dotted line) at  $\varepsilon = 16.43$  suppresses chaos with increasing  $\varepsilon$  and finally becomes stable against filamentary oscillations for  $\varepsilon > 20.2$ , and further on determines the dynamics of the system.

Using the Benettin algorithm [32] we have calculated the two largest Lyapunov exponents  $\lambda_1$  and  $\lambda_2$  for varying  $\varepsilon$  (Fig. 7). We observe that at most one Lyapunov exponent is positive, while the second one is zero for a chaotic orbit. Taking into account the third largest Lyapunov exponent we can then estimate an upper limit for the fractal dimension of the attractor after Kaplan and

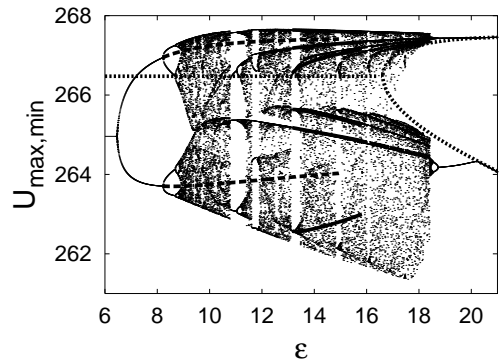


FIG. 6: Bifurcation diagram of maxima and minima of the voltage  $U$  versus  $\varepsilon$ . Thick dotted lines: homogeneous solution; thick dashed lines: period-one breathing orbit, thick solid lines: period-three spiking orbit. Parameters and load line as in Fig. 2(c).

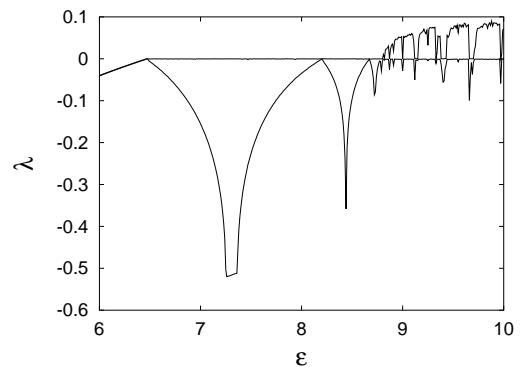


FIG. 7: The two largest Lyapunov exponents as a function of the bifurcation parameter  $\varepsilon$ ; load line as in Fig. 2

Yorke [33] as  $D_{KY} \approx 2.1$ . Although the system has an infinite number of degrees of freedom it is therefore only weakly chaotic. The global coupling is responsible for the suppression of extensive spatio-temporal chaos [34].

#### IV. TIME-DELAYED FEEDBACK CONTROL OF CHAOTIC BREATHING AND SPIKING

We now apply chaos control to stabilize a particular UPO of period  $\tau$  of the uncontrolled system which is embedded in a chaotic attractor. The control forces  $F_a$  and  $F_u$  in eqs. (1),(2) will be designed such that they do not suppress chaos by generating a new periodic solution but only by changing the stability of a solution that already exists in the uncontrolled system. Hence  $F_a$  and  $F_u$  vanish exactly on the target orbit. Such a requirement is in general met by time-delayed feedback schemes [3]. Depending on the particular recipe, which is used for the construction of the control forces, there are various possible control schemes. Here, we are going to analyze four cases which have been already introduced in [16] in the context of reaction-diffusion models with a global

Type of control	$F_a$	$F_u$
diagonal control	$F_{loc}$	$F_{vf}$
global control with voltage feedback	$F_{glo}$	$F_{vf}$
global control without voltage feedback	$F_{glo}$	0
pure voltage control	0	$F_{vf}$
local control without voltage feedback	$F_{loc}$	0

TABLE I: Overview of different control schemes with the corresponding choices of  $F_a$  and  $F_u$

feedback. The model we are investigating in the present manuscript, eqs.(1) and (2), is of much more interest from the point of view of semiconductor physics since it realistically describes a well-known nanostructure device (DBRT). It exhibits a Z-shaped current–voltage characteristic, whereas the model in [16] describes a different semiconductor heterostructure featuring an S-shaped current–voltage characteristic. A comparison with the results of [16] enables us to estimate which properties of the control schemes are robust and do not depend on the particular choice of the model equations. In addition we will find out whether some schemes are particularly useful for application in semiconductor devices. Concerning details of the control schemes the reader may consult [16]. But to keep our presentation self-contained we recall the necessary notation.

We may choose  $F_u = F_{vf}$  with a generic voltage feedback force defined by

$$F_{vf}(t) = u(t) - u(t - \tau) + RF_{vf}(t - \tau). \quad (4)$$

Here  $R$  is a memory parameter which damps sudden changes in the control force by taking into account multiple delays with a decaying weight of earlier states of the system [4]. A control scheme of this type is called extended time-delay autosynchronization (ETDAS). Such a scheme allows for *noninvasive* control, since an unstable state may be maintained with vanishingly small control forces.

For the control force  $F_a$  in the spatial degree of freedom we will alternatively use either a *local* control force,

$$F_{loc}(x, t) = a(x, t) - a(x, t - \tau) + RF_{loc}(x, t - \tau) \quad . \quad (5)$$

where every spatial point is controlled independently of its neighboring points, or a *global* control force

$$F_{glo}(t) = \langle a \rangle(t) - \langle a \rangle(t - \tau) + RF_{glo}(t - \tau) \quad . \quad (6)$$

with  $\langle a \rangle = \frac{1}{L} \int_0^L a dx$  where the same control force is applied to every spatial point. This second choice  $F_a = F_{glo}$  may be experimentally favorable since the spatial average is related to the total charge in the quantum well and does not require a spatially resolved measurement. In the following we will concentrate on the question how the coupling of the control forces to the spatial and discrete degrees of freedom influences the performance of the control. The UPO in question will be a flip orbit, i.e.

its largest complex valued Floquet exponent  $\lambda$  will obey  $\text{Im}\lambda = \pi/\tau$ . This type is practically important, as it naturally arises in period doubling scenarios, and the torsion of the orbit associated with  $\text{Im}\lambda$  is a necessary ingredient for time-delayed feedback control to work [35]. Recently time-delay methods have also been extended to the stabilisation of orbits without torsion by adding a controller associated with an additional unstable degree of freedom [36].

Physically, the control forces may be realized by appropriate electronic control circuits.  $KF_u$  corresponds to an additional control voltage applied in series with the bias  $U_0$ , and  $KF_a$  may be implemented by a spatially extended lateral gate electrode which influences the two-dimensional electron gas in the quantum well locally or globally.

In principle the control performance of time-delayed feedback methods can be studied by linear stability analysis of the differential-delay equations (1),(2) around the target orbit. This is difficult for a general control scheme, since the stability of the orbit is governed by Floquet eigenmodes and by the largest complex valued growth rates  $\Lambda$  (Floquet exponent), which are modified by the control force in a complicated way. Still there exists a particularly simple control scheme, called *diagonal* control [35, 37], for which  $\Lambda(K, R)$  satisfies the exact equation

$$\Lambda + K \frac{1 - e^{-\Lambda\tau}}{1 - Re^{-\Lambda\tau}} = \lambda. \quad (7)$$

where  $\lambda$  is the complex Floquet exponent of the uncontrolled system. Another control scheme for which analytic results are available is the *Floquet mode control* where the control force is a projection onto the unstable Floquet mode [17, 18].

In our model we achieve diagonal control by setting  $F_a = F_{loc}$  and  $F_u = F_{vf}$  (cf. Table I), which is a straightforward extension of the diagonal control for discrete systems (cf. [38]).

We now want to control the period-one orbit (dashed line in Fig. 6) in the chaotic breathing regime (Fig. 4(b)). As explained in Sec. III, this orbit is generated by the supercritical Hopf bifurcation of the stationary filament at  $\varepsilon = \varepsilon_f^h$ . It subsequently becomes unstable by the period doubling cascade with increasing  $\varepsilon$ . From Fig. 8(b) we note that, before the control is switched on ( $K = 0$ ), a sawtooth-like structure in the (fictitious, since not yet applied) control force  $|F|_s = \sup\{|F_{vf}|, |F_{loc}|\}$  appears. This happens as the uncontrolled system approaches and abandons the UPO ergodically. The slope of the increasing control force is given by  $\lambda$ . Such a pattern is useful for tuning the critical parameter  $\tau$  empirically. After the diagonal control is switched on, the control force decays exponentially as  $|F|_s \sim |\exp \Lambda(K, R)t|$  (Fig. 8(b)) to a new level which is about three orders of magnitude smaller than the uncontrolled level. At the same time the voltage signal becomes periodic (Fig. 8(a)), and the chaotic attractor in the phase portrait collapses to a one

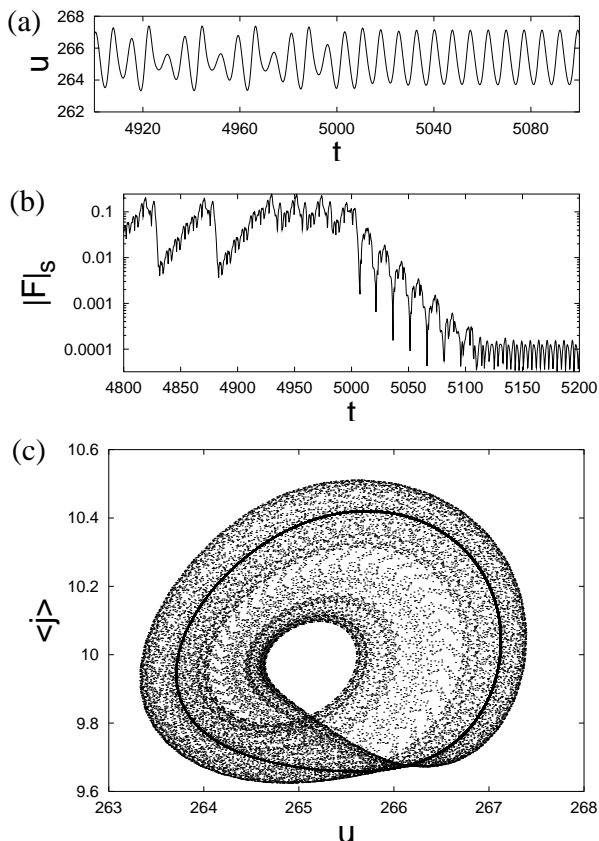


FIG. 8: Diagonal control in the DBRT, where the control force is switched on at  $t = 5000$ . (a) Voltage  $u$  vs. time, (b) Supremum of the control force vs. time, (c) Phase portrait (global current vs. voltage) showing the chaotic breathing attractor and the embedded stabilized periodic orbit (thick solid curve). Parameters:  $r = -35$ ,  $\varepsilon = 9.1$ ,  $\tau = 7.389$ ,  $K = 0.137$ ,  $R = 0$ .

dimensional periodic orbit.

By changing the control parameters  $K$  and  $R$  we observe that the regime of successful control in the  $K$ - $R$  plane (Fig.9(a)) exhibits a typical triangular shape, bounded by a flip instability ( $\text{Re } \Lambda = 0$ ,  $\text{Im } \Lambda = \pi/\tau$ ) to its left and by a Hopf (torus) bifurcation to its lower right. These two boundaries may also be obtained by solving eq. (7) for  $\text{Re } \Lambda = 0$ . We find that the analytical prediction for the control boundaries are in excellent agreement with the numerical results (see Fig. 9(a)).

To confirm the bifurcations at the boundaries we consider the real part of the Floquet spectrum of the orbit subjected to control for varying  $K$  and  $R = 0$  (Fig. 9(b)). Complex conjugate Floquet exponents show up as doubly degenerate pairs. The largest nontrivial exponent decreases with increasing  $K$  and collides at negative values with a branch coming from negative infinity. As a result a complex conjugate pair develops and the real part increases again. The real part of the exponent finally crosses the zero axis giving rise to a Hopf bifurcation.

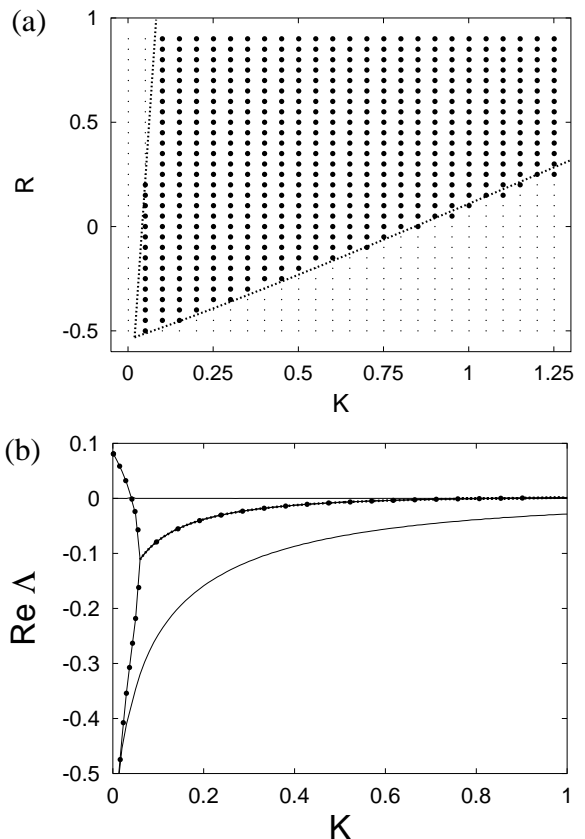


FIG. 9: (a) Control domains in the  $K$ - $R$  parameter plane for diagonal control of the unstable periodic orbit of Fig. 4(b) with period  $\tau = 7.389$ .  $\bullet$  denotes successful control in the numerical simulation,  $\cdot$  denotes no control, lines: analytical result according to eq. (7). (b) Leading real parts  $\Lambda$  of the Floquet spectrum for diagonal control in dependence on  $K$  ( $R = 0$ ), the dotted line denotes a complex conjugate pair of Floquet exponents.  $\bullet$  denotes analytical results from eq. (7).

The numerical simulations agree well with the analytical result.

We now replace the local control force  $F_a = F_{loc}$  by the global control  $F_a = F_{glo}$  without changing the voltage feedback (i.e. global control with voltage feedback in table I). Fig. 10 shows the corresponding control regime and Floquet spectrum. The control domain looks similar in shape as for diagonal control, although the domain for the global scheme is drastically reduced. The shift in the control boundaries is due to a different scenario in the Floquet spectrum. Now  $\text{Re } \Lambda$  decreases more slowly with increasing  $K$  than in the diagonal case, and thus the flip bifurcation takes place at large values of  $K$ . At the same time the complex conjugate pair responsible for the Hopf bifurcation crosses the zero axis with a larger slope and therefore at a smaller  $K$  value than in the diagonal case.

It is now interesting to note that if we keep  $F_a = F_{glo}$  as before but remove the voltage feedback completely, the

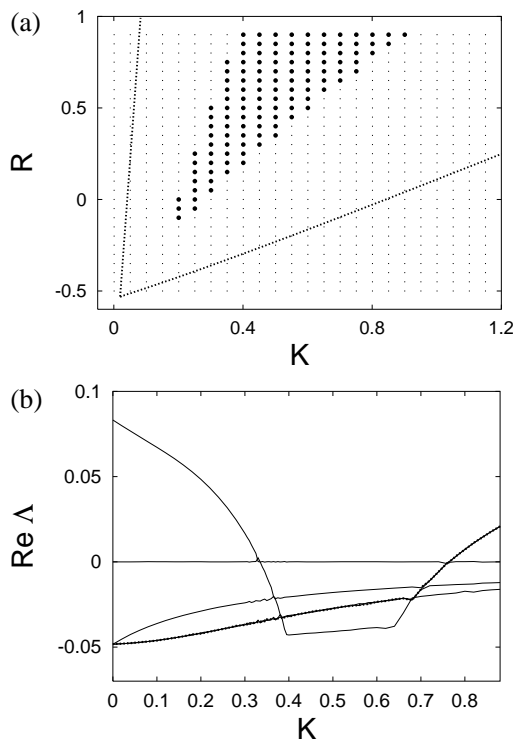


FIG. 10: Same as Fig. 9 for global control with voltage feedback ((b):  $R = 0.7$ )

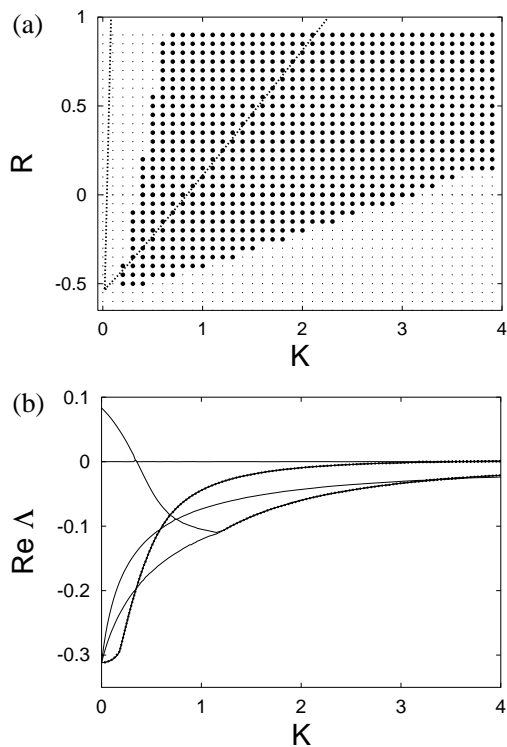


FIG. 11: Same as Fig. 9 for global control without voltage feedback ((b):  $R = 0.1$ ). Note that the scale of the  $K$ -axis is changed.

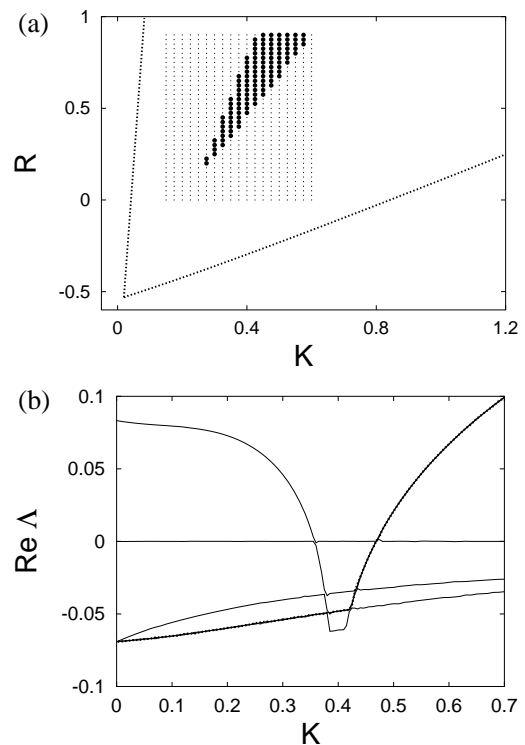


FIG. 12: Same as Fig. 9 for pure voltage control ((b):  $R = 0.6$ )

control domain is shifted to higher  $K$  values and at the same time is dramatically increased (Fig. 11(a)). From the Floquet spectrum we see that after the flip bifurcation the largest Floquet exponent does not immediately hybridize into a complex conjugate pair, but the Hopf bifurcation is caused by another complex conjugate pair which is not connected to the largest Floquet exponent. Thereby the Hopf bifurcation is suppressed and the control regime is increased. This behavior is very similar to the one observed in a different reaction–diffusion model (modeling a heterostructure hot electron diode, HHED) [16], where it was found that additional control of the global variable  $u$  may gradually reduce the control regime to zero.

From the practical point of view the most relevant control scheme is the pure voltage control, i.e.  $F_u = F_{vf}$ ,  $F_a = 0$ , since the voltage variable may be conveniently measured and manipulated by an external electronic device. The corresponding control domain and Floquet exponents are shown in Fig. 12. Here the control regime is even somewhat smaller than in the case of global control with voltage feedback but the shape of the control regime and the Floquet spectrum are qualitatively very similar. It is encouraging that this kind of control is at all possible, since it opens up the opportunity to conveniently study chaos control in a real world device.

We finally consider the case of local control without voltage feedback (Fig. 13). Here the control regime is surprisingly even larger than for diagonal control. The

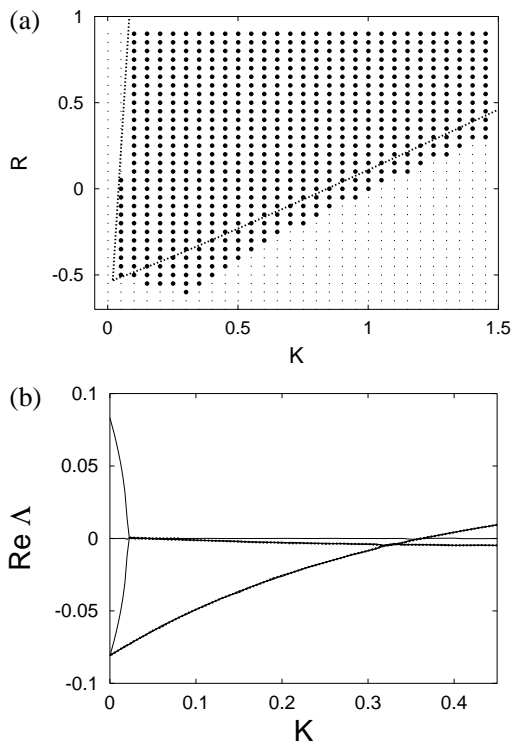


FIG. 13: Same as Fig. 9 for local control without voltage feedback ((b):  $R = -0.55$ ).

shape of the control regime is not triangular any more as before, but has an additional edge at low  $K$  and  $R$  values. The reason for this edge can be explained from the Floquet diagram. Here a Floquet exponent from below collides with the largest Floquet exponent at positive real values before the flip bifurcation occurs. This complex conjugate pair then crosses the zero axes from above and undergoes an inverse Hopf bifurcation. For larger values of  $K$  another complex conjugate pair performs a second Hopf bifurcation seemingly unrelated to the first one.

An overview of the different coupling schemes considered in this section is given in table I. By comparing the different control schemes, we may characterize the influence of the voltage control. If the voltage control is switched on, the largest Floquet exponent rises quickly after the collision with an exponent coming from below, and participates in the Hopf bifurcation at the right boundary of the control regime. If on the other hand the voltage control is switched off, the largest Floquet exponent only rises slowly after the collision, and often the Hopf bifurcation at the right boundary is caused by a complex conjugate pair which is independent of the largest Floquet exponent. In this case the Hopf boundary is shifted to larger values of  $K$  than for diagonal control. The choice of the control force  $F_a$  influences the decrease of  $\text{Re}\Lambda(K)$  at small  $K$ . For  $F_a = F_{\text{loc}}$  this decrease is large and the flip boundary practically coincides with the one obtained for diagonal control, while for  $F_a = F_{\text{glo}}$  the flip boundary is shifted to higher  $K$

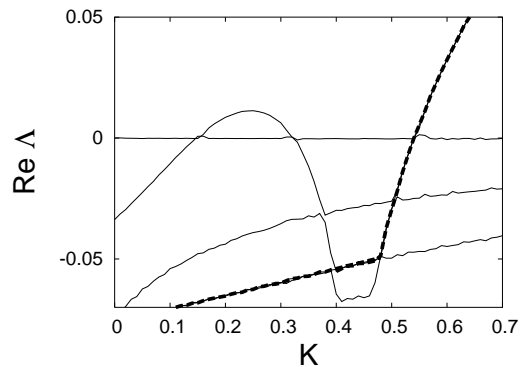


FIG. 14: Leading real parts  $\Lambda$  of the Floquet spectrum for pure voltage control of a stable period-one breathing orbit in dependence on  $K$  ( $R = 0.6$ ,  $\varepsilon = 8.0$ )

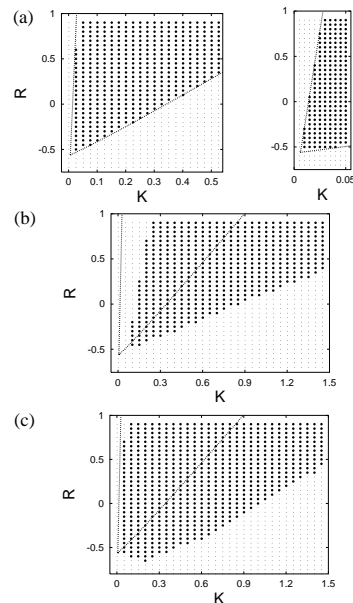


FIG. 15: Control domains for spiking orbit. Lines: analytical results for diagonal control. (a) diagonal control, (b) global control without voltage feedback, (c) local control without voltage feedback (Parameters:  $\varepsilon = 13.44$ ,  $\tau = 20.15$ )

values since  $|\partial_K \text{Re}\Lambda(K)|$  is small. For  $F_a = 0$  the slope  $|\partial_K \text{Re}\Lambda(K)|$  is even smaller, shifting the boundary to even higher  $K$  values.

So far we have stabilized the period-one breathing orbit. We have investigated whether the obtained results are specific for a given UPO, or whether similar results can be observed for different orbits such as the period-three spiking orbit (cf. thick solid lines in Figs. 5,6) which stands for the second basic dynamical pattern (spiking) in the DBRT system. Fig. 15 shows the control regimes for different control schemes. Again we note that diagonal control is very well predictable by the analytic formula (7) (Fig. 15(a)), whereas omitting the voltage control shifts the Hopf border to large  $K$  values, and replacing local with global control shifts the flip bound-

ary to larger  $K$  values. For pure voltage control and global control with voltage feedback no domain of control was found. Nevertheless features of the different control schemes are similar for both breathing and spiking orbits.

## V. TRACKING AND DEPENDENCE OF THE CONTROL PERFORMANCE ON THE LYAPUNOV EXPONENT

Having stabilized periodic orbits for a particular set of parameter values one is in addition able to follow such an orbit through a continuous change of a parameter. Such a kind of tracking is quite common in control of chaos and has been demonstrated even in the context of time-delayed feedback control. The period-one breathing orbit can be controlled continuously in a whole range of values of  $\varepsilon$  (cf. thick dashed lines in Fig. 6 for diagonal control). Note that since the period  $\tau$  of the UPO depends on  $\varepsilon$ ,  $\tau$  needs to be readjusted while sweeping  $\varepsilon$ . It is then even possible to stabilize the period-one orbit in higher periodic windows, where the target orbit is obviously not part of the attractor. This opens up the possibility of obtaining stable self-sustained voltage oscillations independently of parameter fluctuations. The Floquet exponent  $\lambda$  also depends on  $\varepsilon$ , and this allows us to study the control performance as a function of the largest Floquet exponent of the UPO. Thus through the tracking scheme we are also able to study the influence of the Lyapunov exponent on the control performance and to compare the result with recent theoretical predictions [37].

In Fig. 16(a) the control performance for global control with voltage feedback for fixed  $R$  is plotted. As expected, the regime of control is considerably smaller than the analytical predictions for diagonal control. Fig. 16(b) shows the control performance for pure voltage feedback and different values for  $R$ . Although the control regimes are much smaller than predicted for diagonal control, the trend in the shift of the control regime for increasing  $R$  is qualitatively similar.

Surprisingly we find a finite  $K$  value for the flip boundary as  $\lambda\tau \rightarrow 0$  (Fig. 16(b)). This is in marked contrast to the analytical results for diagonal control, where the flip boundary extrapolates to zero for  $\lambda\tau \rightarrow 0$ . To understand why this is the case, let us consider a situation where we apply pure voltage control to a *stable* orbit. From the Floquet spectrum in Fig. 14 we see that with increasing control force the stable orbit is destabilized by a flip bifurcation, then becomes stable again by a second flip bifurcation, before it finally undergoes the usual Hopf bifurcation at high  $K$  values. Such a reentrance scenario does not happen for diagonal control.

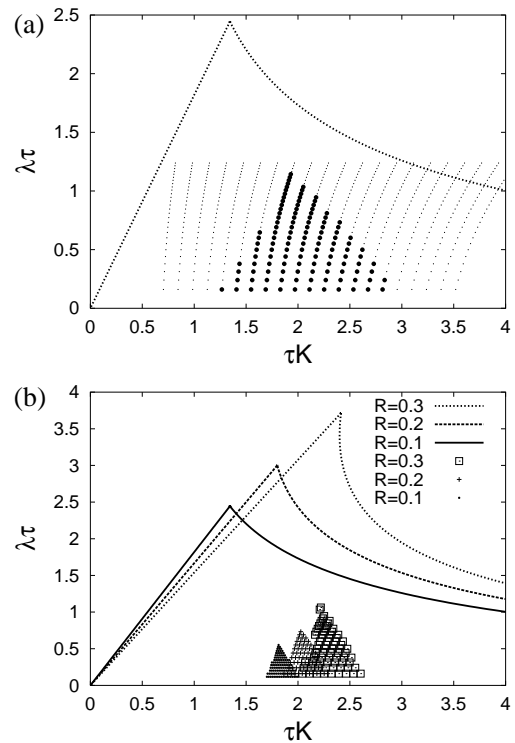


FIG. 16: Control domain in the  $\lambda - K$  plane (a) for global control with voltage feedback ( $R = 0.1$ ),  $\bullet$ : simulation; dotted line: analytical result for diagonal control from eq. (7), (b) pure voltage control (symbols: simulation with different values of  $R$  as given in the legend; lines: analytical results for diagonal control from eq. (7)).

## VI. CONCLUSIONS

We have applied different schemes of chaos control by time-delay autosynchronization to a globally coupled reaction-diffusion model describing charge transport in a semiconductor nanostructure, viz. a double-barrier resonant tunneling diode (DBRT). The spatio-temporal dynamics and bifurcation scenarios of the uncontrolled DBRT in an external circuit display a variety of complex patterns, including breathing and spiking oscillations either of which can be periodic or chaotic.

We have shown that by using time-delayed feedback methods it is possible to stabilize unstable breathing or spiking patterns. Different control schemes were compared with respect to efficiency, and quantitative comparisons of their respective control domains in the  $R - K$  parameter space were given and interpreted in terms of the Floquet spectra. Those turned out to be helpful to gain insight into the control mechanisms and understand why the control performance may, e.g., be improved by omitting control of the voltage variable. Our findings confirm the results obtained previously for a different model [16] on a qualitative level. Inclusion of the voltage feedback in the control scheme has the tendency to reduce the control performance. But for the model system

studied here, which is better adapted to the semiconductor context, we find that even pure voltage feedback is sufficient for successful control. Thus, as a control scheme which is particularly simple to realize experimentally, albeit with a small control regime which requires careful adjustment of the control parameters  $R$  and  $K$ , we have singled out pure voltage control. Our findings may be important for obtaining stable self-sustained voltage oscillations in resonant tunneling diodes independently of parameter fluctuations.

This work was supported by DFG in the framework of Sfb 555.

## APPENDIX A

In this Appendix we provide analytical expressions for the functions  $D(a)$  and  $f(a, u)$  appearing in eq. (1) and relate the dimensionless quantities used throughout this paper to their respective dimensional physical quantities marked by a tilde.

The voltage drop across the DBRT  $\tilde{u}(t)$  and the external bias voltage  $\tilde{U}_0$  are related to their dimensionless counterparts by  $u = e\tilde{u}/(k_B T)$  and  $U_0 = e\tilde{U}_0/(k_B T)$ , respectively, with the temperature  $T$ , the electron charge  $e < 0$ , and Boltzmann's constant  $k_B$ . The two-dimensional electron density is rescaled via  $a = \tilde{a}\pi\hbar^2/(mk_B T)$ , where  $m$  is the effective mass of the electron in the well. Time and space coordinates are rescaled by  $t = \tilde{t}\Gamma_L/\hbar$  and  $x = \tilde{x}/\sqrt{\hbar\mu k_B T}/(-e\Gamma_L)$  where  $\Gamma_L = \Gamma_R$  is the transition rate for electrons from the emitter to the quantum well (and from the quantum well to the collector) and  $\mu$  is the electron mobility.

This yields a rescaling of current and resistance as  $j = \tilde{j}\pi\hbar^3/(emk_B T\Gamma_L)$  and  $r = \tilde{r}e^2mA\Gamma_L/(\pi\hbar^3)$ , respectively, where  $A$  is the cross sectional area of the device. Note that the effective resistance in general contains two terms  $\tilde{r} = R - k$ , where  $R$  represents an external resistor and  $k$  arises from an active circuit with a voltage gain  $U_c =$

$k\tilde{j}A$  [27]. In the case  $k > R$  this leads to  $r < 0$  with particularly interesting chaotic scenarios, as shown in the main text. The time-scale ratio is given by  $\varepsilon = RC\Gamma_L/\hbar$ , where  $C$  is the total capacitance of the circuit.

The effective diffusion coefficient  $D(a)$  may be calculated by considering a generalized form of Einstein's relation which covers the full range from Fermi-degenerate to nondegenerate conditions and a drift term resulting from the change in the local potential due to Poisson's equation [29]:

$$D(a) = a \left( \frac{d}{r_B} + \frac{1}{1 - \exp[-a]} \right), \quad (\text{A1})$$

where  $r_B \equiv (4\pi\epsilon\epsilon_0\hbar^2)/(e^2m)$  is the effective Bohr radius in the semiconductor material,  $\epsilon$  and  $\epsilon_0$  are the relative and absolute permittivity of the material, respectively, and  $d$  is the effective thickness of the double-barrier structure.

The function  $f(a, u)$  is obtained from a microscopic consideration of the tunneling currents  $J_{ew}(a, u)$  and  $J_{wc}(a)$  from the emitter to the quantum well and from the well to the collector, respectively [25]:

$$f(a, u) = \left[ \frac{1}{2} + \frac{1}{\pi} \arctan \left( \frac{2}{\gamma} \left( x_0 - \frac{u}{2} + \frac{d}{r_B} a \right) \right) \right] \times \left[ \ln \left( 1 + \exp \left( \eta_e - x_0 + \frac{u}{2} - \frac{d}{r_B} a \right) \right) - a \right] - a \quad (\text{A2})$$

Here  $\gamma$  and  $x_0$  describe the broadening and the energy level of the electron states in the quantum well, and  $\eta_e$  is the dimensionless Fermi level in the emitter, all in units of  $k_B T$ . In this article we choose  $\gamma = 6$ ,  $d/r_B = 2$ ,  $\eta_e = 28$  and  $x_0 = 114$ . Typical physical values correspond to units of time, space, voltage, electron density, and current density of the order of 3.3 ps, 100 nm, 0.35 mV,  $10^{10} \text{ cm}^{-2}$ ,  $500 \text{ A cm}^{-2}$ , respectively, for  $d = 20 \text{ nm}$ ,  $\Gamma_L = \Gamma_R = 0.2 \text{ meV}$ ,  $k_B T = 0.32 \text{ meV}$  ( $T = 4 \text{ K}$ ).

- 
- [1] E. Ott, C. Grebogi, and J. A. Yorke, *Phys. Rev. Lett.* **64**, 1196 (1990).
- [2] H. G. Schuster, *Handbook of chaos control* (Wiley-VCH, Weinheim, 1999).
- [3] K. Pyragas, *Phys. Lett. A* **170**, 421 (1992).
- [4] J. E. S. Socolar, D. W. Sukow, and D. J. Gauthier, *Phys. Rev. E* **50**, 3245 (1994).
- [5] S. Bielawski, D. Derozier, and P. Glorieux, *Phys. Rev. E* **49**, R971 (1994).
- [6] T. Pierre, G. Bonhomme, and A. Atipo, *Phys. Rev. Lett.* **76**, 2290 (1996).
- [7] C. Simmendinger and O. Hess, *Phys. Lett. A* **216**, 97 (1996).
- [8] K. Hall, D. J. Christini, M. Tremblay, J. J. Collins, L. Glass, and J. Billette, *Phys. Rev. Lett.* **78**, 4518 (1997).
- [9] D. W. Sukow, M. E. Bleich, D. J. Gauthier, and J. E. S. Socolar, *Chaos* **7**, 560 (1997).
- [10] P. Parmananda, R. Madrigal, M. Rivera, L. Nyikos, I. Z. Kiss, and V. Gáspár, *Phys. Rev. E* **59**, 5266 (1999).
- [11] O. Lüthje, S. Wolff, and G. Pfister, *Phys. Rev. Lett.* **86**, 1745 (2001).
- [12] H. Benner and W. Just, *J. Kor. Phys. Soc.* **40**, 1046 (2002).
- [13] C. Beta, M. Bertram, A. S. Mikhailov, H. H. Rotermund, and G. Ertl, *Phys. Rev. E* **67**, 046224 (2003).
- [14] E. Schöll and K. Pyragas, *Europhys. Lett.* **24**, 159 (1993).
- [15] G. Franceschini, S. Bose, and E. Schöll, *Phys. Rev. E* **60**, 5426 (1999).
- [16] O. Beck, A. Amann, E. Schöll, J. E. S. Socolar, and W. Just, *Phys. Rev. E* **66**, 016213 (2002).
- [17] N. Baba, A. Amann, E. Schöll, and W. Just, *Phys. Rev. Lett.* **89**, 074101 (2002).

- [18] W. Just, S. Popovich, A. Amann, N. Baba, and E. Schöll, *Phys. Rev. E* **67**, 026222 (2003).
- [19] E. Schöll, *Nonlinear spatio-temporal dynamics and chaos in semiconductors* (Cambridge University Press, Cambridge, 2001).
- [20] B. A. Glavin, V. A. Kochelap, and V. V. Mitin, *Phys. Rev. B* **56**, 13346 (1997).
- [21] D. Mel'nikov and A. Podlivaev, *Semiconductors* **32**, 206 (1998).
- [22] M. N. Feiginov and V. A. Volkov, *JETP Lett.* **68**, 633 (1998).
- [23] M. Meixner, P. Rodin, E. Schöll, and A. Wacker, *Eur. Phys. J. B* **13**, 157 (2000).
- [24] P. Rodin and E. Schöll, *J. Appl. Phys.* (2003), in print.
- [25] E. Schöll, A. Amann, M. Rudolf, and J. Unkelbach, *Physica B* **314**, 113 (2002).
- [26] V. J. Goldman, D. C. Tsui, and J. E. Cunningham, *Phys. Rev. Lett.* **58**, 1256 (1987).
- [27] A. D. Martin, M. L. F. Lerch, P. E. Simmonds, and L. Eaves, *Appl. Phys. Lett.* **64**, 1248 (1994).
- [28] A. Wacker and E. Schöll, *J. Appl. Phys.* **78**, 7352 (1995).
- [29] V. Cheianov, P. Rodin, and E. Schöll, *Phys. Rev. B* **62**, 9966 (2000).
- [30] A. S. Mikhailov, *Foundations of Synergetics Vol. I*, 2 ed. (Springer, Berlin, 1994).
- [31] S. Bose, P. Rodin, and E. Schöll, *Phys. Rev. E* **62**, 1778 (2000).
- [32] G. Benettin, L. Galgani, A. Giorgilli, and J. Strelcyn, *Meccanica* **15**, 9&21 (1980).
- [33] J. L. Kaplan and J. A. Yorke, in *Functional differential equations and approximations of fixed points. Lecture notes in mathematics Vol. 730*, edited by H. O. Peitgen and H. O. Walter (Springer, Berlin, 1979).
- [34] M. Meixner, S. M. Zoldi, S. Bose, and E. Schöll, *Phys. Rev. E* **61**, 1382 (2000).
- [35] W. Just, T. Bernard, M. Ostheimer, E. Reibold, and H. Benner, *Phys. Rev. Lett.* **78**, 203 (1997).
- [36] K. Pyragas, *Phys. Rev. Lett.* **86**, 2265 (2001).
- [37] W. Just, E. Reibold, H. Benner, K. Kacperski, P. Fronczak, and J. Holyst, *Phys. Lett. A* **254**, 158 (1999).
- [38] M. E. Bleich and J. E. S. Socolar, *Phys. Lett. A* **210**, 87 (1996).